TORC1 signaling exerts spatial control over microtubule dynamics by promoting nuclear export of Stu2

Babet van der Vaart,[1,2] Josef Fischböck,[1] Christine Mieck,[1] Peter Pichler,[1] Karl Mechtler,[1] René H. Medema,[2] and Stefan Westermann[1,3]

[1]Research Institute of Molecular Pathology, Vienna Biocenter, Vienna, Austria
[2]Division of Cell Biology, The Netherlands Cancer Institute, Amsterdam, Netherlands
[3]Department of Molecular Genetics, Faculty of Biology, Center for Medical Biotechnology, University of Duisburg-Essen, Essen, Germany

The target of rapamycin complex 1 (TORC1) is a highly conserved multiprotein complex that functions in many cellular processes, including cell growth and cell cycle progression. In this study, we define a novel role for TORC1 as a critical regulator of nuclear microtubule (MT) dynamics in the budding yeast *Saccharomyces cerevisiae*. This activity requires interactions between EB1 and CLIP-170 plus end–tracking protein (+TIP) family members with the TORC1 subunit Kog1/Raptor, which in turn allow the TORC1 proximal kinase Sch9/S6K1 to regulate the MT polymerase Stu2/XMAP215. Sch9-dependent phosphorylation of Stu2 adjacent to a nuclear export signal prevents nuclear accumulation of Stu2 before cells enter mitosis. Mutants impaired in +TIP–TORC1 interactions or Stu2 nuclear export show increased nuclear but not cytoplasmic MT length and display nuclear fusion, spindle positioning, and elongation kinetics defects. Our results reveal key mechanisms by which TORC1 signaling controls Stu2 localization and thereby contributes to proper MT cytoskeletal organization in interphase and mitosis.

Introduction

Target of rapamycin complex 1 (TORC1) is an evolutionarily conserved multiprotein signaling complex that can detect internal and external cues and incorporate them into an output mechanism that controls cell growth and cell cycle progression, among other things (Loewith and Hall, 2011). In the budding yeast *Saccharomyces cerevisiae*, the TORC1 is composed of the Ser/Thr Tor1/2 kinase, Kog1, Tco89, and Lst8 (Loewith et al., 2002; Reinke et al., 2004) and is predominantly localized to the vacuole membrane (Reinke et al., 2004; Urban et al., 2007; Binda et al., 2009), but Tor1 can also be found in the nucleus (Li et al., 2006). The best-characterized downstream TORC1 substrate is the automatic gain control (AGC) kinase Sch9/S6K1 (Urban et al., 2007). TORC1-mediated phosphorylation of Sch9 occurs at the vacuole membrane and is required for Sch9's activity toward its downstream targets (Urban et al., 2007). Budding yeast also possess the TORC1-related TORC2 complex (Tor2, Avo proteins, Bit61, and Lst8), which regulates actin cytoskeleton dynamics (Schmidt et al., 1996, 1997; Loewith et al., 2002). TORC1 activity can be specifically inhibited by the drug rapamycin, to which TORC2 is mostly insensitive (Loewith et al., 2002). Previously, TORC1 inhibition by rapamycin was reported to affect mitotic spindle elongation, orientation, and kinetics (Choi et al., 2000).

Budding yeast cells undergo a closed mitosis as the nuclear envelope does not disassemble, contrary to vertebrate cells. Proper chromosome segregation depends on mitotic spindle assembly inside the nucleus and the nucleation of cytoplasmic microtubules (MTs) that guide nuclear positioning by interacting with the cell cortex. All yeast MTs, both nuclear and cytoplasmic, are nucleated by the spindle pole body (SPB), the equivalent of the vertebrate centrosome, which is embedded in the nuclear envelope. MT organization and dynamics are partially controlled by highly conserved plus end–tracking proteins (+TIPs) that specifically recognize growing MT plus ends (Akhmanova and Steinmetz, 2015).

The phenotypes reported after TORC1 inhibition were postulated to depend on the +TIP Bik1/CLIP-170 to which Tor1 binds in both budding yeast and mammalian cells (Choi et al., 2000, 2002; Swiech et al., 2011). However, no mechanistic insights into how Tor signaling may influence the MT cytoskeleton have been reported, raising the possibility that the

Correspondence to Stefan Westermann: stefan.westermann@uni-due.de; Babet van der Vaart: b.vd.vaart@nki.nl

Abbreviations used: +TIP, plus end–tracking protein; AGC, automatic gain control; CID, collision-induced dissociation; coIP, coimmunoprecipitation; EBH, end-binding homology; HCD, higher-energy collisional dissociation; IP, immunoprecipitation; iTRAQ, isobaric tag for relative and absolute quantification; MT, microtubule; NES, nuclear export signal; NLS, nuclear localization signal; SEC, size-exclusion chromatography; SPB, spindle pole body; TEAB, triethylammonium bicarbonate; TFA, trifluoroacetic acid.

The Rockefeller University Press
J. Cell Biol. Vol. 216 No. 11 3471–3484
https://doi.org/10.1083/jcb.201606080

previously observed effects may indeed be indirect and merely a consequence of much more general defects, for example in protein synthesis. In addition, the key downstream effectors of TORC1 signaling with regards to MT cytoskeleton regulation have not been identified, and it is unclear whether there is only one or multiple key targets.

In this study, we use the simple, genetically tractable organism budding yeast *S. cerevisiae* to study the role of TORC1-dependent signaling in the regulation of the MT cytoskeleton. We identified Bim1/EB1 and Bik1/CLIP-170 as cell cycle–dependent TORC1 interaction partners, an association mediated by the C terminus of the TORC1 subunit Kog1/Raptor. The TORC1–Bim1/Bik1 interaction brings Stu2/XMAP215 into the vicinity of Sch9/S6K. This kinase phosphorylates Stu2 adjacent to a nuclear export signal (NES), promoting nuclear export and thereby restricting nuclear MT growth. Furthermore, we show that failure to regulate Stu2 nuclear levels in a cell cycle–dependent manner causes nuclear fusion (karyogamy), spindle positioning, and elongation defects.

Results and discussion

TORC1 inhibition in α-factor–arrested cells results in hyperelongation of nuclear MTs

Previously, it was reported that TORC1 inhibition by rapamycin causes karyogamy defects through unknown mechanisms (Choi et al., 2000). Efficient karyogamy requires extensive MT cytoskeleton reorganization with reorientation of cytoplasmic MTs toward the shmoo projection (Molk and Bloom, 2006). To investigate whether TORC1 activity has a role in controlling this morphology, we imaged α-factor–arrested yeast cells expressing Nup60-mCherry to demark the nuclear envelope and GFP-tubulin to visualize the MT cytoskeleton by live microscopy. We analyzed the MT cytoskeleton of a WT cell treated with or without the TORC1-specific inhibitor rapamycin (Fig. 1 A) and deletions of the Tor1 and Tco89 subunits previously shown to inhibit TORC1 signaling (Figs. 1 A and S1 A; Heitman et al., 1991; Loewith et al., 2002). Cytoplasmic MTs of WT cells formed bundles that are attached to and stabilized at the cell cortex, whereas nuclear MTs were short (Fig. 1, A and B). *Tor1Δ* cells often adopted a cell wall polarization defect resulting in a boomerang-shaped cell without a well-defined shmoo projection (Fig. S1 A) and were therefore not considered further. In contrast, cell cycle arrest and shmoo formation were unaffected upon rapamycin treatment and in *tco89Δ* cells, but the MT cytoskeleton was highly abnormal, characterized by hyperelongated nuclear MTs (Fig. 1 A). Excessive nuclear MT growth frequently led to "buckling" upon encountering the distal cortex and caused significant nuclear envelope distortion, a situation never observed under unperturbed conditions (Fig. 1 A). The mean length of nuclear MTs upon rapamycin treatment (2.78 ± 0.07 µm) and in *tco89Δ* cells (3.0 ± 0.47 µm) was >40% longer than that of controls (1.98 ± 0.10 µm), whereas cytoplasmic MT length was unaffected (Fig. 1 B). MT hyperelongation in *tco89Δ* cells was the consequence of fewer catastrophes compared with WT cells (Fig. S1 B). To further dissect the phenotype, we derived an MT polarity index by dividing the number of shmoo tip–oriented MTs with that of cell body–directed MTs in a given time period (Fig. 1 C). Although control cells displayed a preferred MT growth direction toward the shmoo tip (polarity index, 1.97 ± 0.28), this bias was compromised upon rapamycin treatment (1.08 ± 0.14) and, furthermore, was reversed in *tco89Δ* cells (0.76 ± 0.06; Fig. 1 C).

MT dynamics and organization are controlled by +TIPs. Therefore, we analyzed the localization of several +TIPs: Bim1/EB1, Bik1/CLIP-170, and Stu2/XMAP215 as well as Kar3/kinesin-14 and Kar9/APC-like, two previously described Bim1 interaction partners that support MT–shmoo tip attachments (Fig. 1 D; Korinek et al., 2000; Mieck et al., 2015). In α-factor–arrested WT cells, Bim1-, Bik1-, and Stu2-GFP formed comet-like structures predominantly in the cytoplasm directed toward the shmoo projection with only few nuclear GFP-positive plus ends (Fig. 1 D). Interestingly, in *tco89Δ* cells, Bim1-, Bik1-, and Stu2-GFP signals were also highly prominent on nuclear MT ends (Fig. 1 D). The number of nuclear Stu2-positive plus ends of *tco89Δ* cells increased more than twofold (WT, 1.56 ± 0.41; *tco89Δ*, 3.54 ± 0.44; Fig. 1 E). This phenotype was specific for Bik1, Bim1, and Stu2, because Kar3 and Kar9 were exclusively found on cytoplasmic MT plus ends in WT and *tco89Δ* cells (Fig. 1 D). Next, Bim1 and Bik1 contribution to the supernumerary Stu2 nuclear comets phenotype was assessed. *Tco89Δ bim1Δ* and *tco89Δ bik1Δ* double mutants exhibited Stu2-GFP comets in line with the autonomous nature of Stu2 (Fig. 1 F; van Breugel et al., 2003; Podolski et al., 2014). However, Stu2 comets were mostly found proximal to the SPB, the site of MT nucleation, indicating short MTs, in agreement with an MT growth–stimulating role for Bim1 and Bik1 (Berlin et al., 1990; Tirnauer et al., 1999; Blake-Hodek et al., 2010). The reduced cytoplasmic MT length often led to impaired MT–shmoo cortex attachment, causing nuclear displacement (Fig. 1 F, left) as previously reported for Bim1 and Bik1 deletions (Miller et al., 2000; Molk et al., 2006). The total Stu2-GFP comet number was not affected, but the intensity was significantly reduced compared with controls (Fig. 1, E–G), indicating that Bim1 and Bik1 act in synergy with Stu2 to support MT growth as previously reported for XMAP215 and EB1 action (Li et al., 2012; Zanic et al., 2013; Matsuo et al., 2016). In conclusion, these data show that TORC1 inhibition results in hyperelongated nuclear MTs, and this phenotype is Bim1 and Bik1 dependent.

Identification of cell cycle–regulated interactions between +TIPs and TORC1

CLIP proteins and Tor1 have previously been shown to physically interact in budding yeast and human cells (Choi et al., 2000, 2002; Swiech et al., 2011). To investigate the +TIP–TORC1 interaction, we performed low-stringency single-step affinity purifications of Bim1-FLAG and Bik1-FLAG combined with mass spectrometry analysis (Fig. 2, A and B). All TORC1 subunits were copurified with Bim1 and Bik1 as well as many previously described associated partners (Fig. 2 C and Data S1). Reciprocal Tco89 (Tco89-FLAG) and Kog1 (Kog1-FLAG) copurification revealed Bim1-derived peptides, confirming the TORC1–Bim1 interaction (Fig. S1, C and D). Deletion of Bik1 and Bim1, respectively, from Bim1-FLAG and Bik1-FLAG strains slightly decreased the Tco89 interaction in coimmunoprecipitation (coIP) Western blot experiments but did not abrogate it, indicating that these interactions can occur independently of each other (Fig. 2, D and E).

To study the differential affinity of Bim1 interaction partners throughout the cell cycle, cultures were arrested in G1, S, and M phase, and Bim1-FLAG purifications were analyzed by isobaric tag for relative and absolute quantification (iTRAQ) analysis (Fig. S1, E and F; Ross et al., 2004). Interestingly,

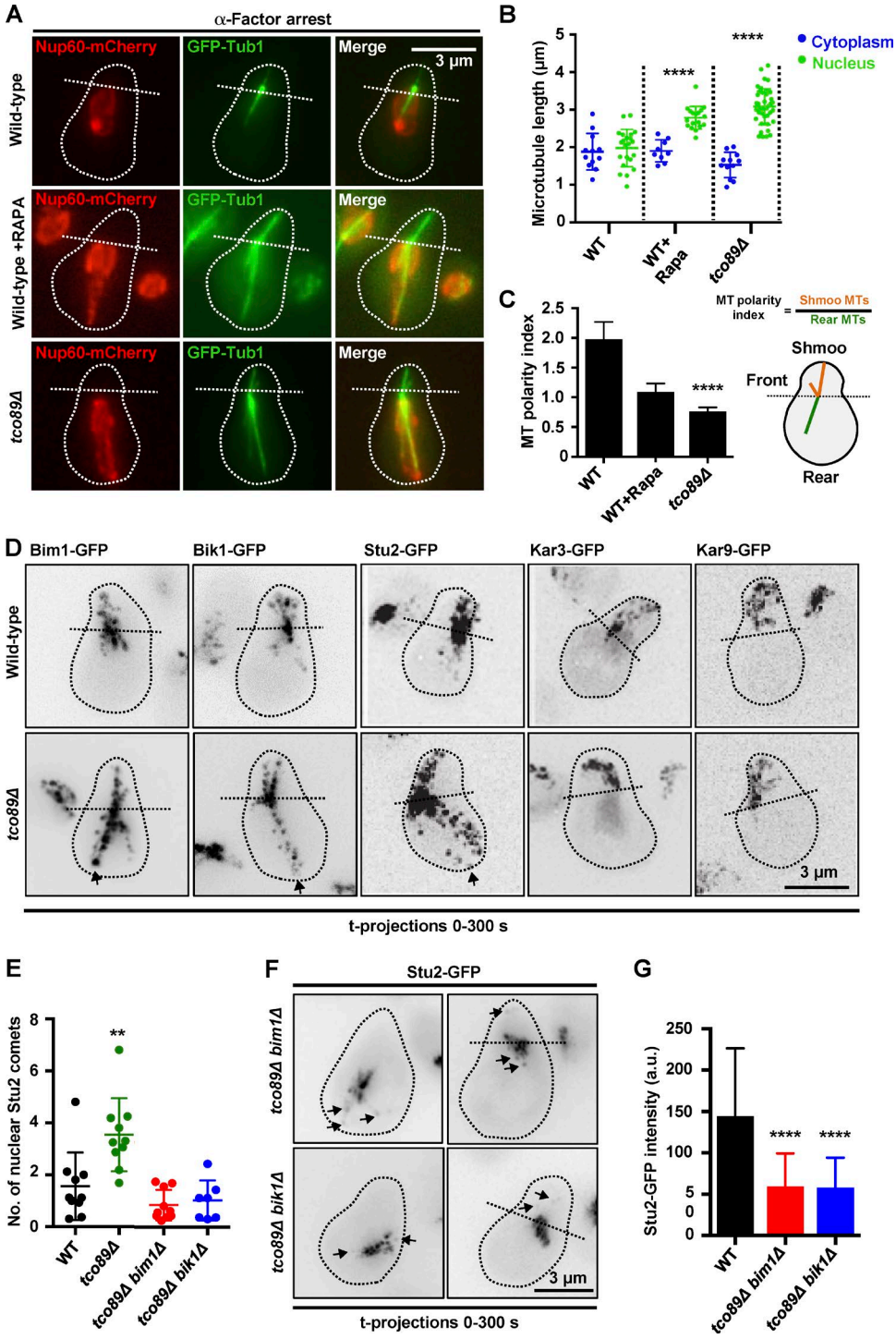

Figure 1. **TORC1 inhibition results in hyperelongated nuclear MTs in polarized yeast cells.** (A) Coimaging of MTs (GFP-Tub1; green) and the nuclear envelope (Nup60-mCherry; red) in α-factor–arrested WT cells with or without rapamycin treatment (30 min at 200 nM) as well as *tco89Δ* cells. Dotted outlines show cell outlines and horizontal lines separate the front and rear of the cell based on SPB position. (B) Graph indicating the length of cytoplasmic and nuclear MTs in the indicated strains. (C) Graph indicating the MT polarity index, defined by the number of shmoo-oriented MTs (orange) divided by the number of rearward oriented nuclear MTs (green) per time frame. A polarity index of one indicates an equal number of MTs growing toward the shmoo and the rear (see scheme on the right). (D) Localization of Bim1-, Bik1-, Stu2-, Kar3-, and Kar9-GFP in WT and *tco89Δ* cells arrested with α-factor. All sixteen frames of a time-lapse video have been projected into a single image to indicate the position of the proteins over time (temporal projection, 300 s total). Arrows indicate nuclear MT ends reaching the rear cortex. Dotted lines separate the front and rear of the cell based on SPB position. (E) Quantification of the number of Stu2-GFP–positive comets in the nucleus of the indicated strains. (F) Temporal projections (all individual frames of a live-cell video projected into one image) of two *tco89Δ bim1Δ* and two *tco89Δ bik1Δ* cells arrested with α-factor–expressing Stu2-GFP. Arrows indicate Stu2-positive comets. Left cells show nuclear displacement caused by impaired MT–shmoo cortex interaction. (G) Quantification of Stu2-GFP comet intensity in WT, *tco89Δ bim1Δ*, *and tco89Δ bik1Δ* double-deletion strains. Data are represented as means ± SEM; **, $P < 0.01$; ****, $P < 0.0001$.

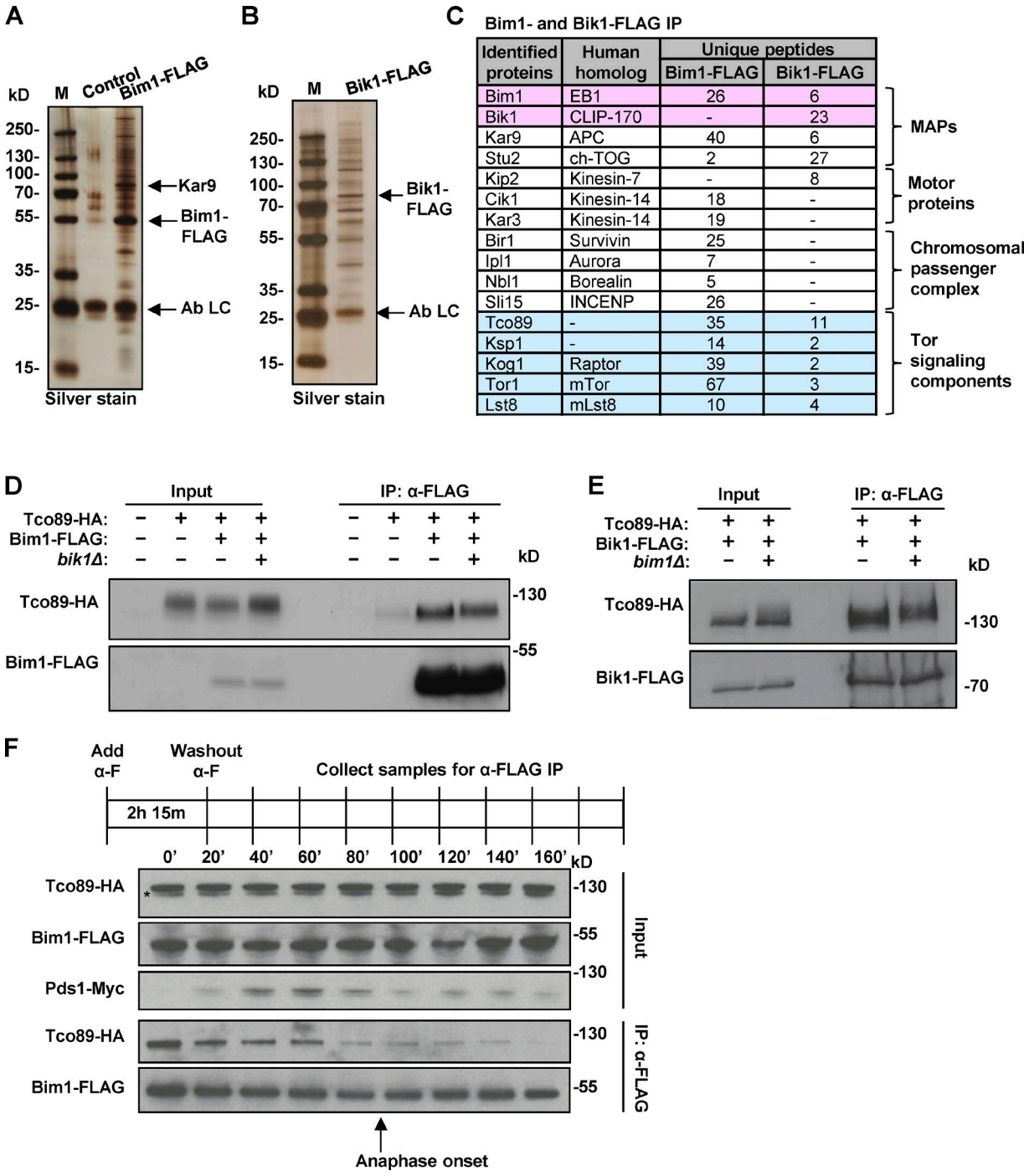

Figure 2. **Cell cycle–regulated interactions between TORC1 and +TIPs.** (A and B) Silver-stained gels of α-FLAG IPs from an untagged control strain or with endogenously tagged Bim1-FLAG (A) as well as a strain with endogenously tagged Bik1-FLAG (B). Identified proteins are indicated. Ab LC, antibody light chain; M, protein marker. (C) Table showing a subset of the identified Bim1-FLAG and Bik1-FLAG partners (See Data S1 for a more complete protein list). The bait proteins Bim1 and Bik1 (pink) and Tor signaling components (blue) are highlighted. In addition to core TORC1 subunits, the Ser/Thr kinase Ksp1 (blue) known to regulate autophagy and filamentous growth and previously implicated in TORC1 signaling was also found (Van Dyke et al., 2006; Umekawa and Klionsky, 2012). It must be noted that although Bik1 is a known Bim1 interaction partner (Wolyniak et al., 2006), it was not identified in this experiment as Bim1’s C-terminal FLAG tag obscures the Bik1 binding site. (D) α-FLAG IPs were performed with extracts of yeast expressing Tco89-HA with or without Bim1-FLAG in the presence or absence of Bik1 and analyzed by Western blotting with α-HA and α-FLAG antibodies. (E) α-FLAG IPs were performed with extracts of yeast expressing Tco89-HA with Bik1-FLAG in the presence or absence of Bim1 and analyzed by Western blotting with α-HA and α-FLAG antibodies. (F) α-FLAG IPs were performed with extracts of yeast cells harvested at different time points after a G1 release expressing Tco89-HA, Bim1-FLAG, and Pds1-Myc and then were analyzed by Western blotting with α-HA, α-FLAG, and α-Myc antibodies. The arrow indicates the onset of anaphase as judged by declining Pds1-Myc protein levels. The asterisk indicates a background band. α-F; α-factor.

TORC1 subunits displayed cell cycle–dependent affinities toward Bim1; their interaction was most prominent during α-factor arrest, whereas it was reduced in S and M phase (Fig. S1 G). To further probe the temporal pattern, we followed the association between Bim1-FLAG and Tco89-HA over the cell cycle by coIP and Western blotting. Confirming the iTRAQ data, the interaction was prominent immediately after α-factor release and remained detectable during S phase, coinciding with maximal Pds1/Securin levels, but was diminished to background in anaphase (Fig. 2 F).

Physical interactions with +TIPs are required for TORC1-mediated control of nuclear MT length

We sought to gain further insights into the TORC1–Bim1/Bik1 binding mechanism. Most EB1/Bim1 partners associate through a small linear peptide motif (SxIP) that binds to the end-binding homology (EBH) domain (Honnappa et al., 2009). To determine whether TORC1 binding involved canonical Bim1-partner interactions, we disrupted SxIP peptide binding by mutating two conserved amino acids (Y220 and E228) to alanines in Bim1 (Bim1-YE/AA; Fig. 3 A; Montenegro Gouveia et al., 2010). Whereas WT Bim1 was able to associate with HA-Kog1, the interaction with the *Bim1-YE/AA* protein was severely compromised (Fig. 3 B). This indicates that Bim1–TORC1 binding is specific and involves interactions of SxIP motif–containing proteins with Bim1's EBH domain. Candidate SxIP motifs (amino acids 335–336 and 368–369) in the unstructured Kog1 N terminus (Fig. S2, A and B) were mutated to asparagines (*kog1-NN*) in a diploid background. However, tetrad dissection failed to recover viable haploid mutant spores (Fig. S2 C), likely explained by impaired TORC1 formation as the *kog1-NN* protein failed to coIP with Tco89-FLAG (Fig. S2 D). We therefore could not use this mutant to address the involvement of Kog1 SxIP sites in Bim1 binding in vivo.

Sequence alignments revealed a conspicuous feature in several *Ascomycota* Kog1 proteins; a conserved, highly acidic and aromatic C-terminal tail reminiscent of the carboxy terminus of the α-tubulins Tub1/3, Bim1, Bik1, and the mammalian SLAIN proteins (Figs. 3 C and S2 E). In these proteins, the aromatic residues confer binding to CAP-Gly domains found in Bik1/CLIP-170 (Honnappa et al., 2006; Weisbrich et al., 2007; van der Vaart et al., 2011). To test the implication of the Kog1 C terminus in +TIP–TORC1 interactions, a *kog1ΔYF* mutant was generated lacking the two aromatic C-terminal residues (Fig. 3 C). The *kog1ΔYF* mutant protein coimmunoprecipitated with Tco89, showing that TORC1 formation was unaffected (Fig. 3 D). Next, we asked whether TORC1-dependent signaling is affected in this mutant by studying the localization of the downstream TOR effector Sfp1 as readout. Normally, this transcription factor resides mostly in the nucleus but relocates to the cytoplasm upon TORC1 inhibition (Fig. 3 E; Jorgensen et al., 2004; Marion et al., 2004; Singh and Tyers, 2009). In *kog1ΔYF* mutants, Sfp1-GFP was nuclear, indicating that TORC1-dependent signaling was not generally impaired (Fig. 3 E). In coIPs, HA-tagged *kog1ΔYF* protein displayed a decreased interaction with Bik1-FLAG, which was not further reduced in a *bim1Δ* background (Fig. 3 F). Importantly, TORC1 complexes containing *Kog1ΔYF* also displayed an impaired Bim1–FLAG interaction in immunoprecipitation (IP) experiments (Fig. 3 G). This could be explained by a cooperative action of Bim1 and Bik1 at the MT plus end. The characterization of the *kog1ΔYF* allele allowed us to specifically probe the contribution of physical +TIP–TORC1 interactions to MT cytoskeleton regulation. If these are required, we would expect the *kog1ΔYF* allele to phenocopy rapamycin treatment. Consistent with this hypothesis, α-factor–arrested GFP-tubulin–expressing *kog1ΔYF* cells showed hyperelongated MTs (2.72 ± 0.08 µm; Fig. 3, H and I) similar to rapamycin treatment or Tco89 deletion (Fig. 1, A and B). Tco89 deletion from the *kog1ΔYF* strain to generate a double mutant (*tco89Δ kog1ΔYF*) had no additive effect on nuclear MT length (3.20 ± 0.10 µm; Fig. 3 I). Collectively, we found that an intact Bim1 EBH domain is necessary for TORC1 binding, and the C-terminal aromatic residues of Kog1 are required for the Bim1 and Bik1 interaction as deletion of these residues severely compromises interactions with both proteins and results in hyperelongated nuclear MTs.

A Stu2 NES is required to restrict nuclear MT length

What may underlie the excessive nuclear MT growth in *tco89Δ* and *kog1ΔYF* mutant cells? MT growth speed is partially controlled by the MT polymerase Stu2/XMAP215, which collaborates with end-binding proteins in growth control (Zanic et al., 2013; Matsuo et al., 2016). Live-cell microscopy revealed that nuclear Stu2-GFP comet number in *tco89Δ* (3.54 ± 0.44) and *kog1ΔYF* (3.27 ± 0.31) cells was greatly increased (Fig. 1, D and E; and Fig. 4 C). Previously, TORC1 activity has been shown to regulate the nucleocytoplasmic transport of transcription factors such as the Rtg1–Rtg3 complex (Komeili et al., 2000), Gln3, and Gar1 (Beck and Hall, 1999). We hypothesized that the observed MT phenotype might be caused by differences in Stu2 nuclear–cytoplasmic shuttling. Nuclear export of proteins is mediated by the binding of a hydrophobic, often leucine-rich NES to the nuclear export receptor exportin-1 (Xpo1) or the chromosome region maintenance 1 protein (Crm1; Fischer et al., 1995; Wen et al., 1995). Stu2 was previously identified in a screen for Xpo1/Crm1 interactors (Kırlı et al., 2015), and it has a putative class 1a/3 NES in its C-terminal tail (amino acids 816–829; I-x_2-L-x_3-V-x_2-L-x_1-I; Fig. 4 A; Fung et al., 2017), in line with the hypothesis that Stu2 is actively exported from the nucleus. We found that mutating the key hydrophobic NES residues to alanines (*stu2-*NES*; amino acids 816–829; I-x_2-L-x_3-A-x_2-A-x_1-A) resulted in hyperelongated nuclear MTs (WT, 1.98 ± 0.10 µm; *stu2-*NES*, 2.83 ± 0.10 µm; Fig. 4, A–C) and increased numbers of nuclear Stu2-*NES-GFP–decorated plus ends (3.33 ± 0.19; Fig. 4, D and E), phenocopying the *tco89Δ* and *kog1Δ*YF mutants (Fig. 1, A, B, D, and E; and Fig. 3, H and I). In support of the idea that misregulated nucleocytoplasmic transport of Stu2 underlies the MT phenotype, we found that fusing a strong nuclear localization signal (NLS) to Stu2 (Stu2-NLS-GFP) was sufficient to promote Stu2 nuclear accumulation as it also resulted in a strong increase in nuclear GFP-positive comets (3.53 ± 0.11; Fig. 4, D and E). In conclusion, a Stu2 C-terminal hydrophobic NES is required for Stu2 nuclear export, and unpermitted Stu2 nuclear accumulation induces nuclear MT hyperelongation in α-factor–arrested cells.

The TORC1-proximal kinase Sch9 is required for nuclear export by phosphorylating Stu2 adjacent to the NES

How does TORC1 activity regulate nuclear export of Stu2 and thus nuclear MT growth? Phosphorylation can positively regulate NESs (la Cour et al., 2004). A recent proteomics study

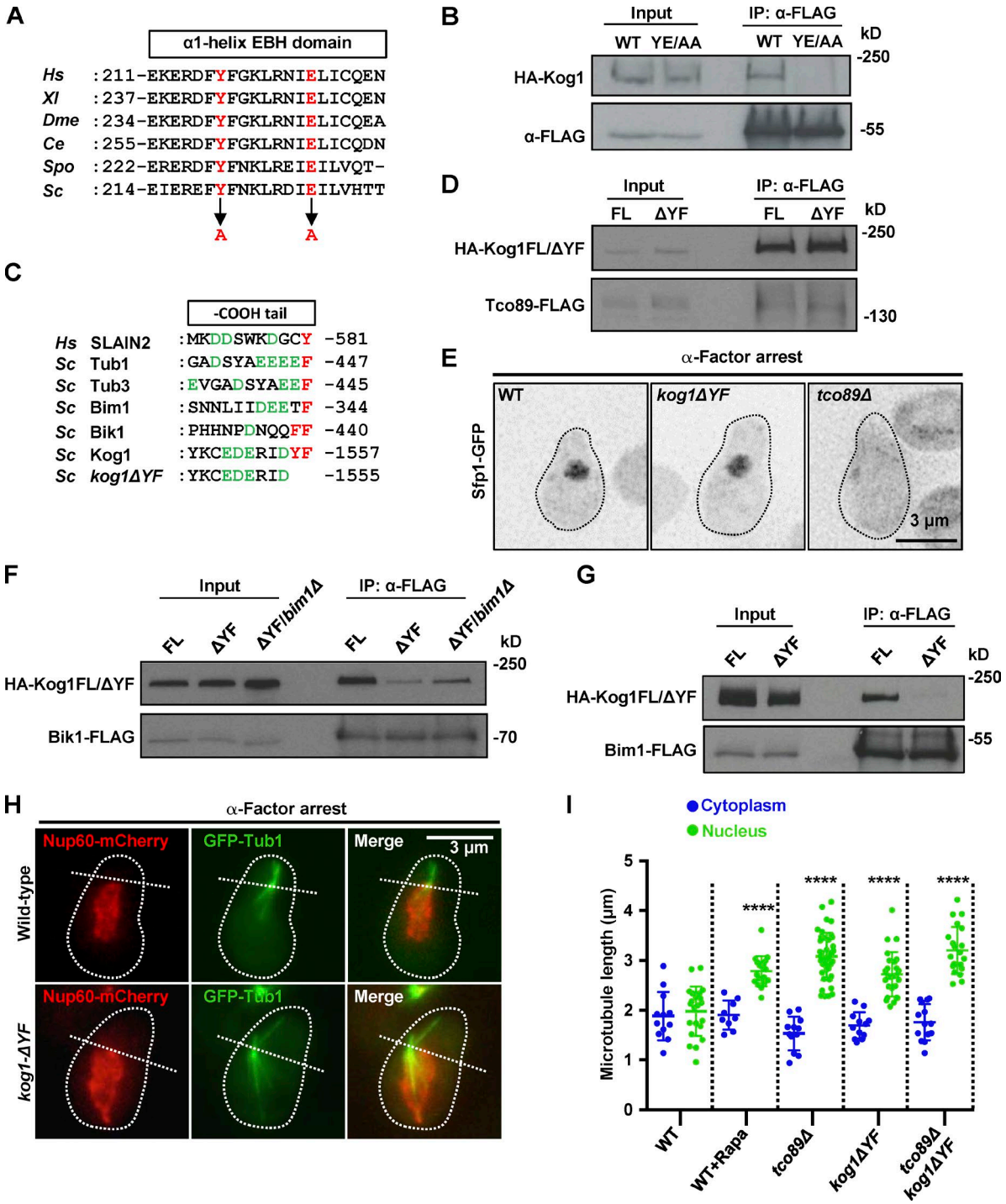

Figure 3. **A Kog1 C-terminal mutant compromises TORC1–Bim1/Bik1 interactions and causes abnormal nuclear MT dynamics.** (A) Sequence alignment of the α1 helix of the EBH domain (required for SxIP motif interactions) of different EB1 species. Mutated amino acids to alanines are highlighted in red. (B) α-FLAG IPs were performed with extracts of yeast cells expressing HA-Kog1 and WT or mutant (YE/AA) Bim1-FLAG and analyzed by Western blotting with α-HA and α-FLAG antibodies. (C) Alignment of the carboxy termini of the indicated proteins. Negatively charged and aromatic residues are highlighted in green and red, respectively. *Ce, Caenorhabditis elegans*; *Dme, Drosophila melanogaster*; *Hs, Homo sapiens*; *Spo, Saccharomyces pombe* (fission yeast); *Sc, S. cerevisiae* (budding yeast); *Xl, Xenopus laevis*. (D) α-FLAG IPs were performed with extracts of yeast expressing Tco89-FLAG and full-length (FL) or C-terminally truncated (*ΔYF*) HA-Kog1 and analyzed by Western blotting with α-HA and α-FLAG antibodies. (E) α-Factor–arrested WT, *HA-kog1ΔYF* (*kog1ΔYF*), and *tco89Δ* cells expressing endogenously tagged Sfp1-GFP. (F) α-FLAG IPs were performed with extracts of yeast expressing Bik1-FLAG, full-length, or mutated (*ΔYF*) HA-Kog1 in the presence or absence (*bim1Δ*) of Bim1 and analyzed by Western blotting with α-HA and α-FLAG antibodies. (G) α-FLAG IPs against Bim1-FLAG were performed with extracts of yeast expressing full-length or mutated (*ΔYF*) HA-Kog1 and analyzed by Western blotting with α-HA and α-FLAG antibodies. (H) Coimaging of MTs (GFP-Tub1; green) and the nuclear envelope (Nup60-mCherry; red) in α-factor–arrested WT cells and *kog1ΔYF* cells. Dotted lines separate the front and rear of the cell based on SPB position, and dotted outlines indicate cell outlines. (I) Graph indicating the length of cytoplasmic (blue) and nuclear (green) MTs in the indicated strains. Data are represented as means ± SEM; ****, $P < 0.0001$.

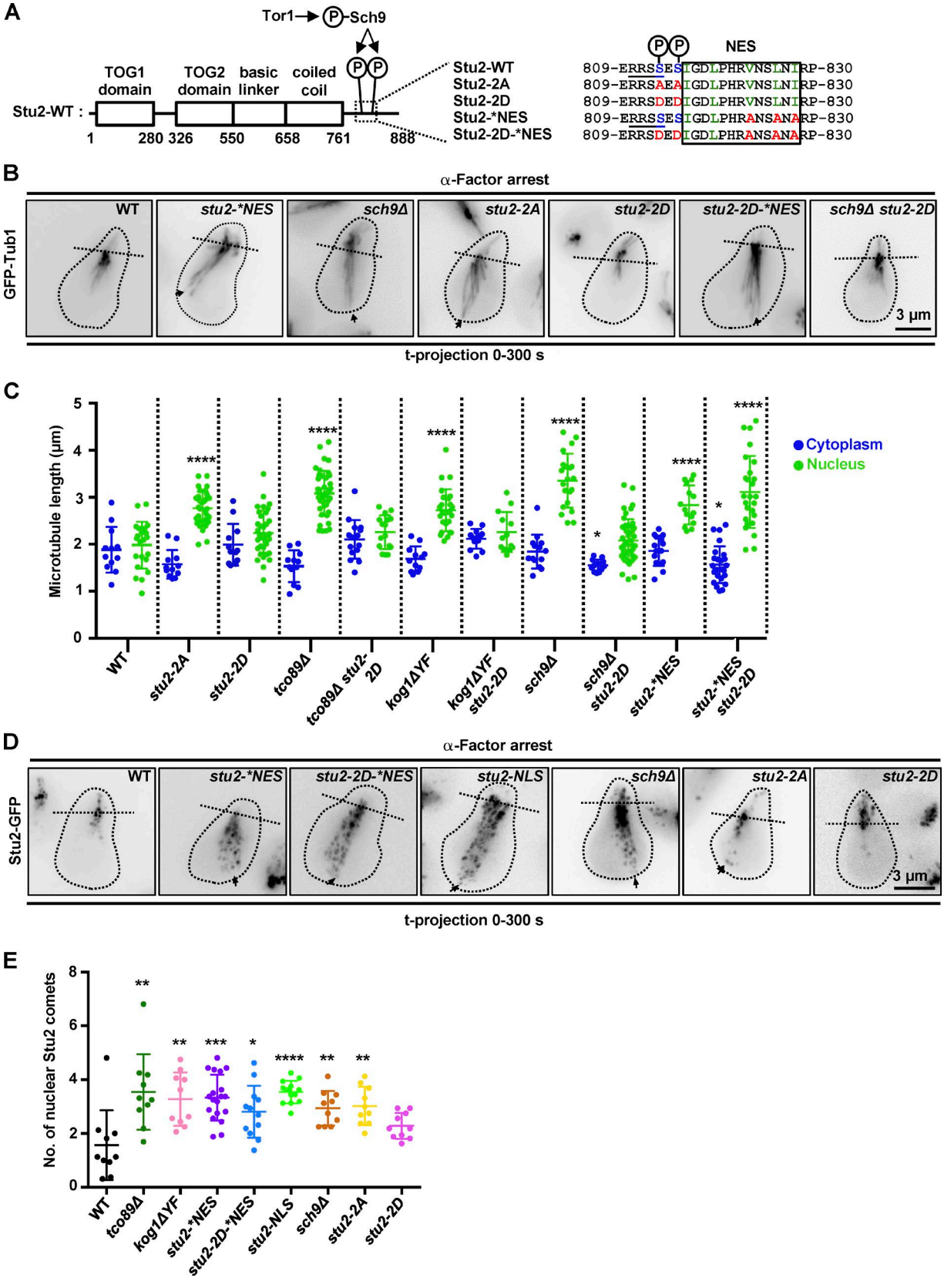

Figure 4. **The TORC1 proximal kinase Sch9/S6K mediates phosphoregulation of Stu2 and restricts nuclear MT growth.** (A) Schematic depiction of Stu2 protein organization. The previously identified Sch9-targeted phospho-sites are indicated in blue (S813 and S815), and the predicted Sch9 consensus site is underlined (RRxS*; amino acids 810–813; Oliveira et al., 2015). NES is boxed (amino acids 816–828), and highlighted in green are the key hydrophobic residues. In red are the mutated residues to generate the indicated Stu2 mutants. Tor1-mediated phosphoactivation of Sch9 is required before it can target its substrates. (B) Temporal projections (all individual frames of a live-cell video projected into one image) of WT, Stu2 NES mutant (*stu2-*NES*),

described the rapamycin-sensitive phosphorylation of two serine residues (amino acids 813 and 815) in the C terminus of Stu2, adjacent to the NES (amino acids 816–829) by Sch9/S6K1 activity (Fig. 4 A; Oliveira et al., 2015). Sch9 is a proximal downstream effector kinase of TORC1, and its activity requires previous TORC1 phosphorylation occurring under favorable growth conditions (Urban et al., 2007). Stu2 phosphorylation at these sites in vivo was also reported by other genomewide phosphoproteomic analyses (Albuquerque et al., 2008; Holt et al., 2009; Soulard et al., 2010; Jones et al., 2011; Swaney et al., 2013). We next addressed the role of Sch9 and the identified Stu2 C-terminal phosphorylation sites in regulating nuclear MT length. Strikingly, Sch9 deletion (*sch9Δ*) or introduction of a phosphorylation-deficient Stu2 mutant allele (*stu2-2A*, *S813A S815A*) led to hyperelongated nuclear MT formation (*sch9Δ*, 3.35 ± 0.57 µm; *stu2-2A*, 2.76 ± 0.35 µm; Fig. 4, B and C) phenocopying TORC1 mutant alleles and the export-compromised *stu2-*NES* (Fig. 1, A and B; Fig. 3, H and I; and Fig. 4, B and C). Consistent with this MT phenotype, *sch9Δ* and *stu2-2A* mutant cells displayed increased Stu2-GFP nuclear comets numbers (*sch9Δ*, 2.93 ± 0.20; *stu2-2A*, 3.01 ± 0.22; Fig. 4, D and E). In contrast, a phosphomimetic Stu2 mutant (*stu2-2D*, *S813D S815D)* displayed MT lengths and Stu2-GFP comet numbers similar to WT cells (2.23 ± 0.08 µm and 2.28 ± 0.15 µm, respectively; Fig. 4, B–E). Moreover, the hyperelongated MT phenotype of *tco89Δ*, *kog1ΔYF*, and *sch9Δ* cells could be suppressed by expression of the *stu2-2D* allele, indicating that the phosphomimetic mutation of these sites is sufficient to restrict MT growth (*tco89Δ stu2-2D*, 2.25 ± 0.08 µm; *kog1ΔYF stu2-2D*, 2.25 ± 0.11 µm; *sch9Δ stu2-2D*, 2.07 ± 0.06 µm; Fig. 4, B and C). Interestingly, the MT phenotype of *stu2*NES* cells could not be rescued by additional phosphomimetic mutations (*stu2*NES*, 2.83 ± 0.10 µm; *stu2-2D-*NES*, 3.11 ± 0.15 µm), indicating that an intact NES is required for Sch9 phosphorylation-driven Stu2 nuclear export (Fig. 4, B–E). Control of the NES is probably the only relevant function for phosphorylation of these residues, as we could not detect significant differences between recombinant WT Stu2 and Stu2-2D proteins in the ability to bind Bik1 (Fig. S3, A and B) or to cosediment with taxol-stabilized MTs (Fig. S3, C and D).

TORC1-dependent regulation of Stu2 nuclear levels is required for proper nuclear fusion, spindle positioning, and elongation

MT polarization toward the shmoo tip and subsequent cortical attachment promotes nuclear conjugation to form a diploid cell (Molk and Bloom, 2006). To evaluate the consequences of defective TORC1-mediated nuclear MT growth control in the mating pathway, we performed genetic crosses where both parental strains contained TORC1 mutant alleles and scored nuclear fusion efficiency. When compared with control, the *tco89Δ* and *kog1ΔYF* single and *tco89Δ kog1ΔYF* double mutants displayed karyogamy defects: ∼46%, ∼36%, and ∼51%, respectively, of cells were delayed or completely failed to fuse their nuclei (Fig. 5 A). Although being significant, these defects were, as expected, less severe than *bim1Δ*, which prevented karyogamy almost completely (∼96%; Fig. 5 A).

The nuclear fusion defects could be explained by nuclear membrane distortion/integrity problems caused by excessive nuclear MT growth. Alternatively, or in addition, reduced cytoplasmic Stu2, Bim1, and Bik1 levels could affect proper cytoplasmic MT dynamics or antiparallel MT bundle organization required for nuclear congression and fusion (Molk and Bloom, 2006). Collectively, these results indicate that excessive nuclear MT polymerization upon inhibited TORC1-dependent signaling or disrupted +TIP–TORC1 interaction interferes with proper karyogamy.

The TORC1–Bim1 interaction is also detectable in cycling cells, particularly during S phase (Fig. 2 F). Therefore, we asked whether compromised +TIP–TORC1 interactions affect the MT cytoskeleton in cycling cells. Growth assays showed that *tco89Δ* or *tco89Δ kog1ΔYF* double mutants grew more slowly on rich medium but conferred a slight growth advantage in the presence of benomyl (MT-depolymerizing drug), consistent with hyperelongated MTs being more benomyl resistant (Fig. 5 B). In 43.0% and 29.8% of *tco89Δ* and *kog1ΔYF* cells, respectively, spindle elongation to >4 µm occurred while the spindle was still positioned in the mother cell. In contrast, only 10% of WT spindles did not reach the bud–neck axis before elongating to 4 µm (Fig. 5, C and D). This is consistent with a previous study on rapamycin treatment affecting the spindle (Choi et al., 2000), and it suggests that TORC1 signaling assists in proper spindle positioning. In budding yeast, two partially redundant pathways control spindle positioning; the Bim1–Kar9–Myo2 pathway (Adames and Cooper, 2000; Hwang et al., 2003) and the dynein pathway (Carminati and Stearns, 1997). The *tco89Δ* and *kog1ΔYF* phenotype is similar to the *dyn1Δ* phenotype as the spindle fails to move into the bud neck and initiates anaphase while still being located entirely in the mother (Eshel et al., 1993; Li et al., 1993). To assess genetically to which pathway TORC1 contributes, *tco89Δ kar9Δ* and *tco89Δ dyn1Δ* double deletion strains were generated and compared with the single deletions. The additional deletion of Tco89 from *dyn1Δ* cells did not have an additive effect compared with *dyn1Δ* cells alone (mispositioning: *tco89Δ dyn1Δ*, 64%; *dyn1Δ*, 62%), whereas the phenotype worsened in *tco89Δ kar9Δ* double mutants compared with *kar9Δ* alone (mispositioning: *kar9Δ*, 40%; *tco89Δ kar9Δ*, 54%), consistent with TORC1 acting in the dynein pathway (Fig. 5 D). Compromised dynein accumulation at cytoplasmic MT ends could be the cause of the TORC1-dependent phenotype as dynein localization is, at least partially, dependent on the cytoplasmic Bik1 level, which is expected to be reduced as a consequence of an increased nuclear level (Fig. 1 D; Eshel et al., 1993; Li et al., 1993; Sheeman et al., 2003). In addition, reduced Stu2 and Bim1 cytoplasmic levels are expected to also negatively affect astral MT growth dynamics, cell cortex interaction, and spindle positioning.

Sch9 deletion (*sch9Δ*), Stu2 phosphodeficient (*stu2-2A*), Stu2 phosphomimetic (*stu2-2D*), Stu2 phosphomimetic and NES mutant (*stu2-2D–*NES*), and *sch9Δ stu2-2D* α-factor–arrested cells expressing GFP-tubulin. Arrows indicate MTs reaching the rear cortex. Dotted lines separate the front and rear of the cell based on SPB position. (C) Graph indicating the length of cytoplasmic (blue) and nuclear (green) MTs in the indicated strains. (D) Localization of Stu2-GFP in the indicated strains arrested with α-factor. Stu2-NLS was generated by fusion of Stu2 to the strong NLS from the viral SV40 large T antigen (PKKKRKV). All sixteen frames of a time-lapse video have been projected into a single image to indicate the position of the proteins over time (300 s total). Arrows indicate MT ends reaching the rear cortex. Dotted lines separate the front and rear of the cell based on SPB position, and dotted outlines indicate cell outlines. (E) Quantification of the number of Stu2-GFP–positive comets in the nuclei of indicated strains. Data are represented as means ± SEM; *, P < 0.05; **, P < 0.01; ****, P < 0.0001.

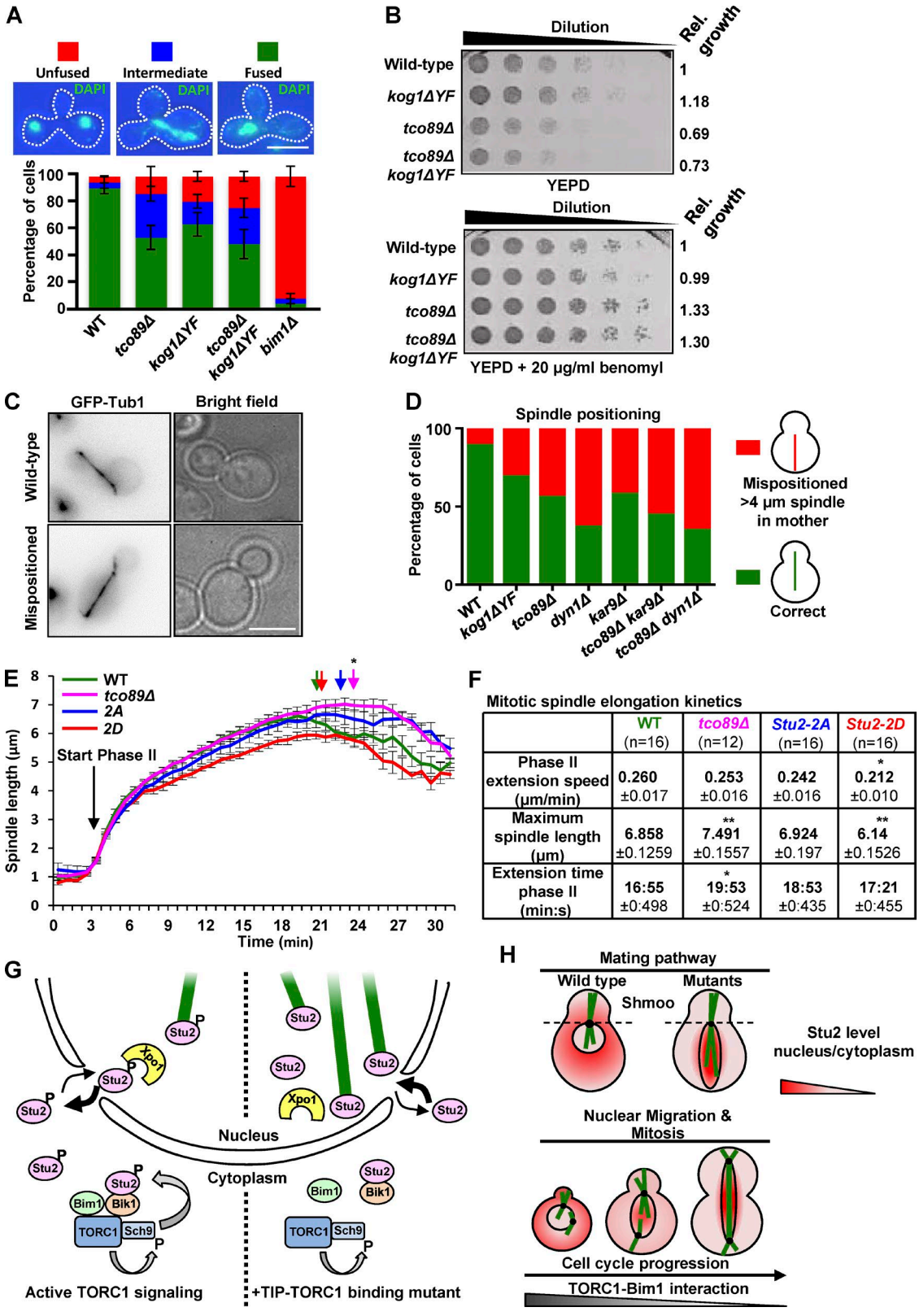

	WT (n=16)	tco89Δ (n=12)	Stu2-2A (n=16)	Stu2-2D (n=16)
Phase II extension speed (µm/min)	0.260 ±0.017	0.253 ±0.016	0.242 ±0.016	* 0.212 ±0.010
Maximum spindle length (µm)	6.858 ±0.1259	** 7.491 ±0.1557	6.924 ±0.197	** 6.14 ±0.1526
Extension time phase II (min:s)	16:55 ±0:498	* 19:53 ±0:524	18:53 ±0:435	17:21 ±0:455

Figure 5. **TORC1-mediated regulation of nuclear MT length is required for proper karyogamy, spindle positioning, and elongation kinetics.** (A) Graph depicts the percentages of the indicated zygotes after mating with unfused (red), fused (green), or intermediate (blue) phenotype nuclei. Representative images of the phenotypes are shown, with DAPI-stained nuclei in green. Dotted outlines indicate cell outlines. (B) Serial dilution growth assays of the indicated strains on rich medium (YEPD) or on medium containing 20 µg/ml benomyl. Growth on plates was quantified by summing up the background-corrected gray values of the dilution series, setting the WT strain to 1. (C) Live-cell imaging of GFP-tubulin to determine spindle position. Examples of a WT or mispositioned mitotic spindle are shown. Note that in mispositioned cells, spindle elongation occurs in the mother. Bars, 3 µm. (D) Quantification of spindle positioning in the indicated strains. (E) Graph indicates spindle elongation kinetics of the indicated strains. Phase II initiation is specified by a black arrow.

To investigate the importance of timely regulation of nuclear versus cytoplasmic Stu2 levels, we analyzed anaphase spindle extension kinetics of WT, *tco89Δ*, *stu2-2A*, and *stu2-2D* cells. Anaphase B consists of two phases: a fast phase I during which overlapping metaphase MTs slide apart (1–2 µm), and a slower phase II where the spindle can further elongate, requiring coupling of antiparallel MT sliding and MT plus end growth (Straight et al., 1997; Khmelinskii et al., 2007). The initial phase I was identical in all tested strains; however, the second phase showed clear differences between WT and mutant cells (Fig. 5, E and F). Spindle elongation kinetics of *stu2-2D* mutant cells were much slower (WT, 0.267 ± 0.005 µm/min; *stu2-2D*, 0.19 ± 0.006 µm/min), and spindles reached a shorter maximum length (WT, 6.858 ± 0.1259 µm; *stu2-2D*, 6.14 ± 0.1526 µm; Fig. 5 F). This result is in line with unpermitted nuclear export of the *stu2-2D* mutant in mitosis, during which normally nuclear Stu2 levels are high, leading to insufficient nuclear Stu2 to support MT growth and mitotic spindle elongation. *Stu2-2A* and *tco89Δ* cells elongated with similar kinetics to WT cells. Although maximum spindle length in the *stu2-2A* mutant was not significantly different from control (WT, 6.858 ± 0.1259 µm; *stu2-2A*, 6.924 ± 0.197 µm), it was increased in *tco89Δ* cells (7.491 ± 0.1557 µm; Fig. 5 F). In support of this finding, *tco89Δ* cells required more time to reach maximum spindle length after phase II initiation (WT, 16:55 min:s ± 0:498 s; *tco89Δ*, 19:53 min:s ± 0:524 s; Fig. 5 F). The increased maximum spindle length in *tco89Δ* cells is in line with overstimulated MT growth caused by increased nuclear Stu2 levels.

In conclusion, these data indicate that failure to export Stu2 from the nucleus results in karyogamy and spindle positioning defects, and it affects spindle elongation kinetics.

A cell needs to exert spatial control over MT dynamics to reorganize the cytoskeleton for different cellular tasks. The problem of local MT dynamics control is particularly pertinent to budding yeast cells, which undergo a closed mitosis, thereby permanently partitioning the cytoskeleton into a nuclear and a cytoplasmic compartment. How cells differentially regulate the cytoskeleton in interphase versus mitosis under these circumstances has remained unclear.

Using the simple, stereotypically arranged MT cytoskeleton of α-factor–arrested yeast cells, we have revealed a surprising role for TORC1 signaling in spatial MT dynamics control (Fig. 5, G and H). We show that TORC1 regulates the MT cytoskeleton by controlling nuclear–cytoplasmic shuttling of the MT growth-stimulating factor Stu2. We demonstrate that TORC1 physically interacts with two +TIPs, Bim1 and Bik1, through its essential subunit Kog1. We propose that these interactions promote the local activation of Sch9 kinase and allow it to phosphorylate its substrate, Stu2 (Fig. 5 G). Sch9 deletion and phosphodeficient Stu2 mutants phenocopy the effect of rapamycin treatment or a +TIP–TORC1 interaction mutant. The observation that the phosphomimetic Stu2 mutant rescues the MT phenotype of all upstream mutants, *sch9Δ*, *tco89Δ*, and *kog1ΔYF*, argues that Stu2 is the key, if not the only, effector in this pathway. Besides Sch9-mediated phosphorylation, an intact NES is also required to promote Stu2 nuclear export, as a Stu2 phosphomimetic mutant was unable to suppress the TORC1-dependent phenotypes in the absence of a functioning NES. Stu2 phosphoregulation may occur in the cytoplasm or at the vacuole membrane, where the concentration of TORC1 components and Sch9 is particularly high (Reinke et al., 2004; Urban et al., 2007; Binda et al., 2009). Failure to detect vacuole localization of Bim1, Bik1, and Stu2 could be explained by the transient interaction between TORC1 and +TIPs. This would be expected because +TIP–EB1 interactions are generally of weak affinity (low micromolar range; Buey et al., 2012). Also, the mean vacuole surface area is large (5–25 µm^2; Chan and Marshall, 2014), resulting in low +TIP concentrations on the vacuole membrane that were possibly below the detection limit of live-cell microscopy. Inversely, we did not observe TORC1 component plus end tracking (not depicted). This might be explained by the high affinity of TORC1 for the vacuole membrane, reducing its diffusion rate and thereby prohibiting plus end–tracking behavior.

The +TIP–TORC1 association is dependent on active TORC1 signaling and is cell cycle regulated (Fig. 5 H). The TORC1–Bim1 interaction is strongly diminished as cells enter mitosis and require Stu2 in the nucleus to build and elongate the mitotic spindle. How temporal control of +TIP–TORC1 interactions is achieved is presently unclear. We note that the phosphorylation state of several TORC1 subunits, including Tco89 changes in response to α-factor (Goranov et al., 2013; unpublished data). The functional integration of TORC1 signaling into the yeast mating pathway will allow a detailed dissection of upstream regulation and downstream effectors in the future.

Collectively, our study has revealed a molecular and functional link between TORC1 and the MT cytoskeleton. We demonstrate that TORC1 induces a cell cycle–dependent switch that allows Stu2 to act on cytoplasmic MTs in interphase and on nuclear MTs in mitosis. With this activity, TORC1 is an important coordinator of MT organization, adding to its key roles during cellular growth.

Materials and methods

Yeast strain construction

Yeast strains (Table S2) are based on the S288C background, and genetic modifications were introduced using standard procedures. *Bim1-YE/AA-FLAG*, HA-Kog1-FL, and *HA-kog1ΔYF* strains were generated by subcloning the 3′ UTR (500 bp), 5′ UTR (500 bp), and the respective ORFs and tags into a pRS306 plasmid (for plasmids, see Table S1). Mutations were introduced using the Phusion Site-Directed Mutagenesis kit (Thermo Fisher Scientific) or QuikChange Multi Site-Directed Mutagenesis kit (Agilent Technologies). Linearized vector constructs were integrated, replacing the endogenous locus. *Stu2-*NES*, *stu2-2A*, and *stu2-2D* mutants were generated by overlapping PCR with primers containing the required mutations and transforming

Colored arrows indicate mean time points of maximum spindle elongation. (F) Table summarizing the indicated parameters. Data are represented as means ± SEM; *, P < 0.05; **, P < 0.01. (G) TORC1-mediated phosphorylation of Sch9 kinase activates it and allows subsequent phosphorylation of its substrate Stu2. This phosphorylation most likely occurs at the vacuole or in the cytoplasm, and it promotes the nuclear exit of Stu2 by the Crm1/exportin-1 (Xpo1). In the +TIP–TORC1 binding mutant, Stu2 is no longer regulated by Sch9-mediated phosphorylation, and intranuclear levels of Stu2 accumulate, resulting in hyperelongation of the MT in this compartment. (H) Stu2 levels in the nucleus versus the cytoplasm are indicated with different intensities (red is high; pink is low). During the yeast mating pathway, nuclear Stu2 levels are normally restricted by active export, whereas in the described mutants, nuclear Stu2 levels increase. As cells enter the cell cycle, the interaction between +TIPs and TORC1 decreases, nuclear Stu2 levels increase, and growth of nuclear spindle MTs are stimulated, all of which are required for proper spindle kinetics.

the PCR product into cells. The *stu2-NLS-GFP* strain was generated by introducing the NLS coding sequence of SV40 large T antigen (PKK KRKV) into the forward PCR primer.

Single-step FLAG purifications from yeast extracts

Desired strains were grown to OD_{600} = 1 for asynchronous cultures or to OD_{600} = 0.5, supplemented with 10 µg/ml final concentration α-factor mating pheromone, 0.2 M (final concentration) hydroxyurea (Sigma-Aldrich), or 15 µg/ml (final concentration) nocodazole (Sigma-Aldrich) and grown for another 2 h 15 min to OD_{600} = 1. Rapamycin (LC Laboratories) and cycloheximide (Sigma-Aldrich) at a final concentration of 200 nM and 25 µg/ml, respectively was added to a culture of OD_{600} = 1 30 min before harvesting. In case of nutrient withdrawal, cells were grown to OD_{600} = 1, spun down, and resuspended in H_2O and then grown another 45 min before harvest. Cells were harvested and either frozen as droplets in liquid N_2 and subsequently lysed with a freezer mill or lysed using glass beads in a mini BeadBeater (Biospec Products). The yeast pellets were dissolved in buffer A (25 mM Hepes, pH 8.0, 2 mM $MgCl_2$, 0.5 mM EGTA, pH 8.0, 0.1 mM EDTA, 0.1% NP-40 [EMD Millipore], 15% glycerol, 150 mM KCl, and 1× protease inhibitor cocktail set IV [EMD Millipore]). The cleared lysate was incubated for 2 h with magnetic DynaBeads (Thermo Fisher Scientific) coupled with α-FLAG M2 antibody (Sigma-Aldrich). Beads were washed three times with buffer B (25 mM Hepes, pH 8.0, and 150 mM KCl) before the beads were resuspended in sample buffer.

Recombinant protein purification

Escherichia coli cells expressing StrepII-TEV-Bik1 were harvested by centrifugation, and bacterial pellets were resuspended in lysis buffer (50 mM Na_2HPO_4/NaH_2PO_4, pH 8, 300 mM NaCl, 2.5% [vol/vol] glycerol, and 0.05% [vol/vol] Tween-20) and disrupted by sonication. After centrifugation, the cleared lysate was incubated with strep-tactin resin and rotated at 4°C for at least 4 h. Bik1 was cleaved off the beads by overnight digest with tobacco etch virus protease, and the flowthrough was collected after passing through disposable columns (Bio-Rad Laboratories). After further purification by gel filtration, aliquots were snap-frozen in liquid N_2 and stored at −80°C.

Plasmids suitable for production of recombinant Stu2-WT-Flag and Stu2-2D-Flag bacmids were generated as described previously (Weissmann et al., 2016). Sf9 cultures were harvested 72 h after infection, and pellets were lysed by Dounce homogenization in 20 mM Na_2HPO_4/NaH_2PO_4, pH 8, 300 mM NaCl, 2.5% (vol/vol) glycerol, and 0.05% (vol/vol) Tween-20. Cleared lysates were incubated with M2-agarose and washed repeatedly with lysis buffer, and then proteins were eluted by incubation of beads with 1 mg/ml 3×Flag peptide in lysis buffer. N-terminally tagged 6×His-Bim1 was purified as described previously (Zimniak et al., 2009). Before analytical size-exclusion chromatography (SEC) experiments, proteins were dialyzed against 20 mM Na_2HPO_4/NaH_2PO_4, pH 6.8, 200 mM NaCl, and 2.5% (vol/vol) glycerol, and SEC was performed in the same buffer.

MT cosedimentation assays were performed as described previously (Zimniak et al., 2009). Proteins were diluted into PEM buffer (80 mM Pipes, pH 6.8, 1 mM $MgCl_2$, and 1 mM EGTA) containing 100 mM NaCl and precleared by centrifugation in a TL100 rotor at 60,000 rpm for 10 min. Final salt concentration in the assay was PEM with 50 mM NaCl.

Antibodies

Antibodies used in this study: monoclonal anti-FLAG M2 (Sigma-Aldrich), anti-FLAG M2 monoclonal antibody peroxidase conjugate (Sigma-Aldrich), monoclonal antibody, HA.11 (Covance), monoclonal antibody anti-HA (clone HA-7; Sigma-Aldrich), monoclonal c-Myc (Covance), and peroxidase-conjugated Affinipure anti–mouse IgG (Jackson ImmunoResearch Laboratories, Inc.).

Live-cell imaging

Log-phase growing cells were arrested with 10 µg/ml α-factor mating pheromone and imaged on concanavalin A (Sigma-Aldrich)–coated culture dishes (MatTek Corporation) or coverslips at room temperature or at 30°C by live-cell DeltaVision deconvolution microscopy (Applied Precision Ltd.) on a microscope (IX-71; Olympus) controlled by SoftWoRx (Applied Precision, Ltd.) and equipped with a 100× oil immersion Plan-Apochromat 1.4 NA objective (Olympus) and a CoolSNAP HQ camera (Photometrics) at 25°C or 30°C. Z stacks (8–12 stacks 0.20 µm apart) were acquired for 5 min at 20-s intervals and projected into 2D images using SoftWoRx and then were further analyzed by MetaMorph (Molecular Devices). Rapamycin (LC Laboratories) at a final concentration of 200 nM was added to a culture of OD_{600} = 1, 15–30 min before imaging. Spindle elongation kinetics were determined by imaging the cells in concanavalin A–coated culture dishes for 35 min with 45-s intervals and analyzed by measuring interspindle pole distance using ImageJ software (National Institutes of Health).

MT polarity index

To obtain the MT polarity index, the number of cytoplasmic, shmoo-oriented, and nuclear rearward growing MTs in a cell per time frame of a 2.5- or 5-min video (8 or 16 frames) were counted. Next, the mean numbers of the 8 or 16 frames were extracted. The ratio was obtained by dividing the number of cytoplasmic MTs with the number of nuclear ones. For each condition, >11 cells were analyzed.

Karyogamy assay

Strains of opposite mating types were grown for 2 h at 30°C in 2 ml of YPD, after which cultures were mixed and centrifuged, and then the pellet was transferred to a YPD plate. Mating was allowed to occur for 4–5 h at 25°C. The mated cells were resuspended in 1 ml of YPD and fixed with 0.1 ml 37% formaldehyde by incubating for 1 h at room temperature with rotation. Cells were washed twice with 1 ml H_2O before being resuspended in 1 ml 70% EtOH and incubated for 30 min with rotation at room temperature. Cells were centrifuged and resuspended in 500 ml H_2O and briefly sonicated before 4 µl of cell suspension was mixed with 4 µl of DAPI containing mounting medium on an imaging coverslip. Nuclei of mated cells were scored as fused, unfused, or intermediate phenotype.

Sample preparation for mass spectrometry analysis

FLAG-purified samples were obtained as described in the Single-step FLAG purifications from yeast extracts section. However, for mass spectrometry analysis, samples were washed three times with buffer A, four times with buffer B, and three times with triethylammonium bicarbonate (TEAB; 50 mM). Subsequently, on-bead digestion was performed in 190 µl TEAB (50 mM) supplemented with 10 µl (100 ng/µl stock) LysC. Incubation proceeded overnight at 37°C at 1,200 rpm. Samples were passed through an Ultrafree MC filter (0.1 µm cutoff; EMD Millipore), and the volume of the samples was reduced to ∼5 µl by evaporation in a speed-vac. Subsequently, 15 µl of 1 M TEAB was added to each sample. Disulfide bonds were reduced by adding Tris(2-carboxyethyl)phosphin to a final concentration of 1 mM and incubation at 60°C for 30 min. Cysteines were blocked by adding methyl methanethiosulfonate to a final concentration of 2 mM and incubation in the dark for 30 min. Tryptic digestion was started by adding 200 ng of trypsin and incubation at 37°C, followed by adding another 200 ng of trypsin 3 h later. For iTRAQ analysis, the four samples, asynchronous, α-factor arrest, hydroxyurea, and nocodazole, were processed separately. 70 µl of ethanol was added

to each vial of iTRAQ 4plex reagent, followed by vortexing. iTRAQ labeling was performed by adding half of the volume of the iTRAQ reagent vial to the respective digested sample and incubation for 2 h at room temperature. Samples were labeled as follows: asynchronous with iTRAQ-114, α-factor arrest with iTRAQ-115, hydroxyurea with iTRAQ-116, and nocodazole with iTRAQ-117. Labeling efficiency was checked by a separate liquid chromatography–mass spectrometry analysis of each sample and searching of the data for variable iTRAQ 4plex modification of peptide N termini and lysines. Labeling was repeated until the labeling efficiency (in terms of the percentage of labeled peptide N-terminal and lysine residues) was >98% for each sample. Eventually, the four labeled iTRAQ samples were mixed in a 1:1:1:1 manner, the combined sample was acidified with trifluoroacetic acid (TFA), and the volume was reduced in a speed-vac to evaporate the ethanol.

FLAG-IP samples destined for the identification of interacting proteins were handled analogous to the iTRAQ samples with minor modifications of the protocol: After on-bead LysC digestion, the volume was not reduced by evaporation in a speed-vac. 4 µl DTT (stock 1 mg/ml) was added to reduce disulfide bonds (30 min at 56°C), and 4 µl methyl methanethiosulfonate (stock 40 mM) was added to alkylate the free thiol groups of cysteines (30 min in the dark). Digestion was started by adding 4 µl of trypsin (100 ng/µl stock) followed by another 4 µl 2 h later, and incubation proceeded at 37°C overnight. For identification analyses, the iTRAQ-labeling step was deliberately omitted. Digestion was stopped by adding 10 µl of 10% TFA.

Peptide separation by nanoHPLC

Peptide separation was performed on an Ultimate 3000 RSLCnano system (Thermo Fisher Scientific) using a 50-cm analytical column (Acclaim PepMap C18; 2 µm, 100 Å, 50 cm × 75 µm). Peptides were first concentrated on a precolumn (Acclaim PepMap C18; 5 µm, 100 Å, 2 cm × 100 µm) using 0.1% TFA as loading solution. After 10 min, the precolumn was switched into the column flow. Data acquisition on the mass spectrometer was started by a contact closure signal 3 min after valve switching. Running solution A was 2% acetonitrile and 0.1% TFA, whereas running solution B was 80% acetonitrile and 0.08% TFA. Depending on the complexity of the sample, one of the following linear gradients was applied: 2% B to 40% B in 60.0 min for phosphorylation analyses, 2% B to 40% B in 120.0 or 180.0 min for identification analyses, or 2% B to 40% B in 240.0 min for iTRAQ quantification analyses. Subsequently, running solution B was increased to 90% B within 5 min and maintained at 90% for further 5 min, and then decreased to 2% B in 2 min followed by column equilibration at 2% B for further 28 min.

Mass spectrometry data acquisition

Data were acquired either on a Velos Orbitrap or on a QExactive mass spectrometer (Thermo Fisher Scientific). Acquisition time was 20.0 min longer than the duration of the 2–40% linear gradient on the RSLC.

Capillary temperature on the Velos Orbitrap instrument was set to 275°C. Internal calibration was based on the polydimethylcyclosiloxane ions at 445.120024 m/z. One mass spectrometry survey scan was acquired at a resolution of 60,000 at 400 m/z with an AGC target value of 1,000,000 ions. For identification analyses, the survey scan was followed by up to 12 collision-induced dissociation (CID) scans excluding singly charged ions, the isolation window was set to 2.0 D, AGC target value was 10,000 ions, normalized collision energy was 35%, and dynamic exclusion ±5 ppm and 30.0 s. For iTRAQ analysis, the survey scan was followed by a maximum of 2 × 5 tandem mass spectrometry scans of the five most intense ions excluding singly charged ions. A hybrid data acquisition method was applied in which both a CID scan (for identification) and a higher-energy collisional dissociation (HCD) scan (for quantification) were acquired for each precursor ion. CID settings were as follows: isolation window 2.40 D, AGC target value 10,000 ions, and normalized collision energy 35%. HCD settings were: isolation window 1.60 D, AGC target value 100,000 ions, and normalized collision energy 40%, and first mass value was fixed to 100 m/z to ensure detection of iTRAQ reporter ions. The dynamic exclusion window was set to ± 5 ppm and 30.0 s.

On the QExactive instrument, capillary temperature was also set to 275°C. The polydimethylcyclosiloxane ions at 445.12003 m/z were used for internal calibration. MS survey scans were acquired at a resolution of 70,000 at 200 m/z with an AGC target value of 1,000,000 ions. The survey scan was followed by up to 10 or 12 tandem mass spectrometry scans of the most abundant ions, excluding singly charged species. Resolution was 17,500 at 200 m/z for tandem mass spectrometry scans. Peptide match and exclude isotopes were set on. For identification, the isolation window was set to 2.0 m/z, and a normalized collision energy of 30% was applied. For iTRAQ analysis, precursor ions were isolated using an isolation window of 1.0 m/z and fragmented by application of a normalized collision energy of 35% capillary electrophoresis. To ensure detection of iTRAQ reporter ions in the iTRAQ analysis, first mass was set to 100 m/z.

Data processing

For the iTRAQ analysis, raw data were searched against the yeast database with Proteome Discoverer (1.4.0.288; Thermo Fisher Scientific) and MASCOT (2.0; Matrix Science). Yeast protein sequences were supplemented with the sequences of common contaminant proteins, and the entire set of sequences was reversed to create a combined forward and decoy database. The following search parameters were applied: enzyme trypsin/P allowing maximum two missed cleavages; MS1 tolerance, 10 ppm; tandem mass spectrometry tolerance, 0.5 D for CID (Velos) and 30 mmu for HCD scans (QExactive); fixed modifications, iTRAQ 4plex N terminus and lysine, Methylthio (Cys); variable modifications, oxidation (M). For data acquired on the QExactive, HCD scans were used for both identification and quantification. For data acquired on Velos Orbitrap, CID scans were used for identification, and HCD scans were used for quantification, respectively. Reporter ion quantification was performed by picking the centroid with the smallest Δ mass within a 7-mmu window with regard to the exact reporter ion m/z. Protein ratios were calculated as the median of peptide ratios and normalized to the bait.

For identification analysis of FLAG-IPs, search parameters were analogous to the iTRAQ analysis; however Methylthio (Cys) was set as the only type of fixed modification. Oxidation of methionine was searched as a variable modification.

For phosphorylation analysis, settings were analogous to the identification analyses, except that phosphorylation of serine, threonine, or tyrosine were included as additional variable modifications. PhosphoRS 2.0 was used for an automated calculation of phosphorylation site probabilities.

For all mass spectrometry results, filter criteria were adjusted for each sample to ensure a low false discovery rate and high data confidence. For instance, iTRAQ peptide–spectrum matches were filtered for search engine rank 1, minimum length 7, MASCOT score 10, and Percolator confidence high q = 0.01 (which corresponds with a false discovery rate of 1%). In addition, protein grouping according to maximum parsimony principle was applied.

The quality of the mass spectrometry data was assessed by several means: First, quality control samples were analyzed before and after the analytical samples, which allowed monitoring the retention times of known peptides and the sensitivity of the liquid chromatography–mass spectrometry system in an automated manner (Pichler et al., 2012). Second, for iTRAQ analysis, labeling efficiency was checked, and the data were normalized based on the protein ratio of the bait

protein. Third, for phosphorylation analysis, spectra were manually inspected and rejected if considered of inadequate spectral quality.

Online supplemental material

Fig. S1 describes the proteomics approach to identify Bim1 interactors. Fig. S2 describes the characterization of molecular features of Kog1. Fig. S3 describes biochemical characterization of WT and mutant Stu2. Table S1 lists plasmids generated and used in this study. Table S2 lists yeast strains used in this study. Data S1 provides a comprehensive list of Bim1 and Bik1 binding partners identified by mass spectrometry.

Acknowledgments

The authors wish to thank Dr. F. van Leeuwen (Netherlands Cancer Institute, Amsterdam, the Netherlands) for sharing the *sch9Δ* strain, Dr. A. Köhler (Max F. Perutz Laboratories, Vienna, Austria) for the Nup60-mCherry plasmid, Alexander Schleiffer for bioinformatics assistance, Susanne Opravil and Johannes Fuchs for mass spectrometry assistance, Otto Hudecz for mass spectrometry data processing assistance, and all members of the Westermann, Medema, and Rowland laboratories for discussions.

Research leading to these results has received funding from the European Molecular Biology Organization Long-Term Fellowship 899-2011 and the Nederlandse Organisatie voor Wetenschappelijk Onderzoek–Aard en Levenswetenschappen–Veni 863.14.006 to B. van der Vaart and the European Research Council under the European Community's Seventh Framework Program (FP7/2007-2013)/European Research Council grant agreement (203499), by the Austrian Science Fund (SFB F34-B03), and the Austrian Research Promotion Agency to S. Westermann. S. Westermann acknowledges support by the Deutsche Forschungsgemeinschaft's collaborative research center CRC1093. Basic research at the Institute of Molecular Pathology is funded by Boehringer Ingelheim.

The authors declare no competing financial interests.

Author contributions: B. van der Vaart, R.H. Medema, and S. Westermann designed the research; B. van der Vaart, J. Fischböck, and C. Mieck prepared reagents; P. Pichler and K. Mechtler performed mass spectrometry analysis; and B. van der Vaart and S. Westermann performed experiments, analyzed data, and wrote the manuscript.

Submitted: 17 June 2016
Revised: 14 February 2017
Accepted: 2 August 2017

References

Adames, N.R., and J.A. Cooper. 2000. Microtubule interactions with the cell cortex causing nuclear movements in Saccharomyces cerevisiae. *J. Cell Biol.* 149:863–874. https://doi.org/10.1083/jcb.149.4.863

Akhmanova, A., and M.O. Steinmetz. 2015. Control of microtubule organization and dynamics: two ends in the limelight. *Nat. Rev. Mol. Cell Biol.* 16:711–726. https://doi.org/10.1038/nrm4084

Albuquerque, C.P., M.B. Smolka, S.H. Payne, V. Bafna, J. Eng, and H. Zhou. 2008. A multidimensional chromatography technology for in-depth phosphoproteome analysis. *Mol. Cell. Proteomics.* 7:1389–1396. https://doi.org/10.1074/mcp.M700468-MCP200

Beck, T., and M.N. Hall. 1999. The TOR signalling pathway controls nuclear localization of nutrient-regulated transcription factors. *Nature.* 402:689–692. https://doi.org/10.1038/45287

Berlin, V., C.A. Styles, and G.R. Fink. 1990. BIK1, a protein required for microtubule function during mating and mitosis in Saccharomyces cerevisiae, colocalizes with tubulin. *J. Cell Biol.* 111:2573–2586. https://doi.org/10.1083/jcb.111.6.2573

Binda, M., M.P. Péli-Gulli, G. Bonfils, N. Panchaud, J. Urban, T.W. Sturgill, R. Loewith, and C. De Virgilio. 2009. The Vam6 GEF controls TORC1 by activating the EGO complex. *Mol. Cell.* 35:563–573. https://doi.org/10.1016/j.molcel.2009.06.033

Blake-Hodek, K.A., L. Cassimeris, and T.C. Huffaker. 2010. Regulation of microtubule dynamics by Bim1 and Bik1, the budding yeast members of the EB1 and CLIP-170 families of plus-end tracking proteins. *Mol. Biol. Cell.* 21:2013–2023. https://doi.org/10.1091/mbc.E10-02-0083

Buey, R.M., I. Sen, O. Kortt, R. Mohan, D. Gfeller, D. Veprintsev, I. Kretzschmar, J. Scheuermann, D. Neri, V. Zoete, et al. 2012. Sequence determinants of a microtubule tip localization signal (MtLS). *J. Biol. Chem.* 287:28227–28242. https://doi.org/10.1074/jbc.M112.373928

Carminati, J.L., and T. Stearns. 1997. Microtubules orient the mitotic spindle in yeast through dynein-dependent interactions with the cell cortex. *J. Cell Biol.* 138:629–641. https://doi.org/10.1083/jcb.138.3.629

Chan, Y.H., and W.F. Marshall. 2014. Organelle size scaling of the budding yeast vacuole is tuned by membrane trafficking rates. *Biophys. J.* 106:1986–1996. https://doi.org/10.1016/j.bpj.2014.03.014

Choi, J.H., N.R. Adames, T.F. Chan, C. Zeng, J.A. Cooper, and X.F. Zheng. 2000. TOR signaling regulates microtubule structure and function. *Curr. Biol.* 10:861–864. https://doi.org/10.1016/S0960-9822(00)00599-6

Choi, J.H., P.G. Bertram, R. Drenan, J. Carvalho, H.H. Zhou, and X.F. Zheng. 2002. The FKBP12-rapamycin-associated protein (FRAP) is a CLIP-170 kinase. *EMBO Rep.* 3:988–994. https://doi.org/10.1093/embo-reports/kvf197

Eshel, D., L.A. Urrestarazu, S. Vissers, J.C. Jauniaux, J.C. van Vliet-Reedijk, R.J. Planta, and I.R. Gibbons. 1993. Cytoplasmic dynein is required for normal nuclear segregation in yeast. *Proc. Natl. Acad. Sci. USA.* 90:11172–11176. https://doi.org/10.1073/pnas.90.23.11172

Fischer, U., J. Huber, W.C. Boelens, I.W. Mattaj, and R. Luhrmann. 1995. The HIV-1 Rev activation domain is a nuclear export signal that accesses an export pathway used by specific cellular RNAs. *Cell.* 82:475–483.

Fung, H.Y., S.C. Fu, and Y.M. Chook. 2017. Nuclear export receptor CRM1 recognizes diverse conformations in nuclear export signals. *eLife.* 6:e23961. https://doi.org/10.7554/eLife.23961

Goranov, A.I., A. Gulati, N. Dephoure, T. Takahara, T. Maeda, S.P. Gygi, S. Manalis, and A. Amon. 2013. Changes in cell morphology are coordinated with cell growth through the TORC1 pathway. *Curr. Biol.* 23:1269–1279. https://doi.org/10.1016/j.cub.2013.05.035

Heitman, J., N.R. Movva, and M.N. Hall. 1991. Targets for cell cycle arrest by the immunosuppressant rapamycin in yeast. *Science.* 253:905–909. https://doi.org/10.1126/science.1715094

Holt, L.J., B.B. Tuch, J. Villén, A.D. Johnson, S.P. Gygi, and D.O. Morgan. 2009. Global analysis of Cdk1 substrate phosphorylation sites provides insights into evolution. *Science.* 325:1682–1686. https://doi.org/10.1126/science.1172867

Honnappa, S., O. Okhrimenko, R. Jaussi, H. Jawhari, I. Jelesarov, F.K. Winkler, and M.O. Steinmetz. 2006. Key interaction modes of dynamic +TIP networks. *Mol. Cell.* 23:663–671. https://doi.org/10.1016/j.molcel.2006.07.013

Honnappa, S., S.M. Gouveia, A. Weisbrich, F.F. Damberger, N.S. Bhavesh, H. Jawhari, I. Grigoriev, F.J. van Rijssel, R.M. Buey, A. Lawera, et al. 2009. An EB1-binding motif acts as a microtubule tip localization signal. *Cell.* 138:366–376. https://doi.org/10.1016/j.cell.2009.04.065

Hwang, E., J. Kusch, Y. Barral, and T.C. Huffaker. 2003. Spindle orientation in Saccharomyces cerevisiae depends on the transport of microtubule ends along polarized actin cables. *J. Cell Biol.* 161:483–488. https://doi.org/10.1083/jcb.200302030

Jones, M.H., J.M. Keck, C.C.L. Wong, T. Xu, J.R. Yates III, and M. Winey. 2011. Cell cycle phosphorylation of mitotic exit network (MEN) proteins. *Cell Cycle.* 10:3435–3440. https://doi.org/10.4161/cc.10.20.17790

Jorgensen, P., I. Rupes, J.R. Sharom, L. Schneper, J.R. Broach, and M. Tyers. 2004. A dynamic transcriptional network communicates growth potential to ribosome synthesis and critical cell size. *Genes Dev.* 18:2491–2505. https://doi.org/10.1101/gad.1228804

Khmelinskii, A., C. Lawrence, J. Roostalu, and E. Schiebel. 2007. Cdc14-regulated midzone assembly controls anaphase B. *J. Cell Biol.* 177:981–993. https://doi.org/10.1083/jcb.200702145

Kırlı, K., S. Karaca, H.J. Dehne, M. Samwer, K.T. Pan, C. Lenz, H. Urlaub, and D. Görlich. 2015. A deep proteomics perspective on CRM1-mediated nuclear export and nucleocytoplasmic partitioning. *eLife.* 4:e11466. https://doi.org/10.7554/eLife.11466

Komeili, A., K.P. Wedaman, E.K. O'Shea, and T. Powers. 2000. Mechanism of metabolic control. Target of rapamycin signaling links nitrogen quality to the activity of the Rtg1 and Rtg3 transcription factors. *J. Cell Biol.* 151:863–878. https://doi.org/10.1083/jcb.151.4.863

Korinek, W.S., M.J. Copeland, A. Chaudhuri, and J. Chant. 2000. Molecular linkage underlying microtubule orientation toward cortical sites in yeast. *Science.* 287:2257–2259. https://doi.org/10.1126/science.287.5461.2257

la Cour, T., L. Kiemer, A. Mølgaard, R. Gupta, K. Skriver, and S. Brunak. 2004. Analysis and prediction of leucine-rich nuclear export signals. *Protein Eng. Des. Sel.* 17:527–536. https://doi.org/10.1093/protein/gzh062

Li, H., C.K. Tsang, M. Watkins, P.G. Bertram, and X.F. Zheng. 2006. Nutrient regulates Tor1 nuclear localization and association with rDNA promoter. *Nature.* 442:1058–1061. https://doi.org/10.1038/nature05020

Li, W., T. Moriwaki, T. Tani, T. Watanabe, K. Kaibuchi, and G. Goshima. 2012. Reconstitution of dynamic microtubules with Drosophila XMAP215, EB1, and Sentin. *J. Cell Biol.* 199:849–862. https://doi.org/10.1083/jcb.201206101

Li, Y.Y., E. Yeh, T. Hays, and K. Bloom. 1993. Disruption of mitotic spindle orientation in a yeast dynein mutant. *Proc. Natl. Acad. Sci. USA.* 90:10096–10100. https://doi.org/10.1073/pnas.90.21.10096

Loewith, R., and M.N. Hall. 2011. Target of rapamycin (TOR) in nutrient signaling and growth control. *Genetics.* 189:1177–1201. https://doi.org/10.1534/genetics.111.133363

Loewith, R., E. Jacinto, S. Wullschleger, A. Lorberg, J.L. Crespo, D. Bonenfant, W. Oppliger, P. Jenoe, and M.N. Hall. 2002. Two TOR complexes, only one of which is rapamycin sensitive, have distinct roles in cell growth control. *Mol. Cell.* 10:457–468. https://doi.org/10.1016/S1097-2765(02)00636-6

Marion, R.M., A. Regev, E. Segal, Y. Barash, D. Koller, N. Friedman, and E.K. O'Shea. 2004. Sfp1 is a stress- and nutrient-sensitive regulator of ribosomal protein gene expression. *Proc. Natl. Acad. Sci. USA.* 101:14315–14322. https://doi.org/10.1073/pnas.0405353101

Matsuo, Y., S.P. Maurer, M. Yukawa, S. Zakian, M.R. Singleton, T. Surrey, and T. Toda. 2016. An unconventional interaction between Dis1/TOG and Mal3/EB1 in fission yeast promotes the fidelity of chromosome segregation. *J. Cell Sci.* 129:4592–4606.

Mieck, C., M.I. Molodtsov, K. Drzewicka, B. van der Vaart, G. Litos, G. Schmauss, A. Vaziri, and S. Westermann. 2015. Non-catalytic motor domains enable processive movement and functional diversification of the kinesin-14 Kar3. *eLife.* 4:e04489. https://doi.org/10.7554/eLife.04489

Miller, R.K., S.C. Cheng, and M.D. Rose. 2000. Bim1p/Yeb1p mediates the Kar9p-dependent cortical attachment of cytoplasmic microtubules. *Mol. Biol. Cell.* 11:2949–2959. https://doi.org/10.1091/mbc.11.9.2949

Molk, J.N., and K. Bloom. 2006. Microtubule dynamics in the budding yeast mating pathway. *J. Cell Sci.* 119:3485–3490. https://doi.org/10.1242/jcs.03193

Molk, J.N., E.D. Salmon, and K. Bloom. 2006. Nuclear congression is driven by cytoplasmic microtubule plus end interactions in S. cerevisiae. *J. Cell Biol.* 172:27–39. https://doi.org/10.1083/jcb.200510032

Montenegro Gouveia, S., K. Leslie, L.C. Kapitein, R.M. Buey, I. Grigoriev, M. Wagenbach, I. Smal, E. Meijering, C.C. Hoogenraad, L. Wordeman, et al. 2010. In vitro reconstitution of the functional interplay between MCAK and EB3 at microtubule plus ends. *Curr. Biol.* 20:1717–1722. https://doi.org/10.1016/j.cub.2010.08.020

Oliveira, A.P., C. Ludwig, M. Zampieri, H. Weisser, R. Aebersold, and U. Sauer. 2015. Dynamic phosphoproteomics reveals TORC1-dependent regulation of yeast nucleotide and amino acid biosynthesis. *Sci. Signal.* 8:rs4. https://doi.org/10.1126/scisignal.2005768

Pichler, P., M. Mazanek, F. Dusberger, L. Weilnböck, C.G. Huber, C. Stingl, T.M. Luider, W.L. Straube, T. Köcher, and K. Mechtler. 2012. SIMPAT IQCO: a server-based software suite which facilitates monitoring the time course of LC-MS performance metrics on Orbitrap instruments. *J. Proteome Res.* 11:5540–5547. https://doi.org/10.1021/pr300163u

Podolski, M., M. Mahamdeh, and J. Howard. 2014. Stu2, the budding yeast XMAP215/Dis1 homolog, promotes assembly of yeast microtubules by increasing growth rate and decreasing catastrophe frequency. *J. Biol. Chem.* 289:28087–28093. https://doi.org/10.1074/jbc.M114.584300

Reinke, A., S. Anderson, J.M. McCaffery, J. Yates III, S. Aronova, S. Chu, S. Fairclough, C. Iverson, K.P. Wedaman, and T. Powers. 2004. TOR complex 1 includes a novel component, Tco89p (YPL180w), and cooperates with Ssd1p to maintain cellular integrity in Saccharomyces cerevisiae. *J. Biol. Chem.* 279:14752–14762. https://doi.org/10.1074/jbc.M313062200

Ross, P.L., Y.N. Huang, J.N. Marchese, B. Williamson, K. Parker, S. Hattan, N. Khainovski, S. Pillai, S. Dey, S. Daniels, et al. 2004. Multiplexed protein quantitation in Saccharomyces cerevisiae using amine-reactive isobaric tagging reagents. *Mol. Cell. Proteomics.* 3:1154–1169. https://doi.org/10.1074/mcp.M400129-MCP200

Schmidt, A., J. Kunz, and M.N. Hall. 1996. TOR2 is required for organization of the actin cytoskeleton in yeast. *Proc. Natl. Acad. Sci. USA.* 93:13780–13785. https://doi.org/10.1073/pnas.93.24.13780

Schmidt, A., M. Bickle, T. Beck, and M.N. Hall. 1997. The yeast phosphatidylinositol kinase homolog TOR2 activates RHO1 and RHO2 via the exchange factor ROM2. *Cell.* 88:531–542. https://doi.org/10.1016/S0092-8674(00)81893-0

Sheeman, B., P. Carvalho, I. Sagot, J. Geiser, D. Kho, M.A. Hoyt, and D. Pellman. 2003. Determinants of S. cerevisiae dynein localization and activation: implications for the mechanism of spindle positioning. *Curr. Biol.* 13:364–372. https://doi.org/10.1016/S0960-9822(03)00013-7

Singh, J., and M. Tyers. 2009. A Rab escort protein integrates the secretion system with TOR signaling and ribosome biogenesis. *Genes Dev.* 23:1944–1958. https://doi.org/10.1101/gad.1804409

Soulard, A., A. Cremonesi, S. Moes, F. Schütz, P. Jenö, and M.N. Hall. 2010. The rapamycin-sensitive phosphoproteome reveals that TOR controls protein kinase A toward some but not all substrates. *Mol. Biol. Cell.* 21:3475–3486. https://doi.org/10.1091/mbc.E10-03-0182

Straight, A.F., W.F. Marshall, J.W. Sedat, and A.W. Murray. 1997. Mitosis in living budding yeast: anaphase A but no metaphase plate. *Science.* 277:574–578. https://doi.org/10.1126/science.277.5325.574

Swaney, D.L., P. Beltrao, L. Starita, A. Guo, J. Rush, S. Fields, N.J. Krogan, and J. Villén. 2013. Global analysis of phosphorylation and ubiquitylation cross-talk in protein degradation. *Nat. Methods.* 10:676–682. https://doi.org/10.1038/nmeth.2519

Swiech, L., M. Blazejczyk, M. Urbanska, P. Pietruszka, B.R. Dortland, A.R. Malik, P.S. Wulf, C.C. Hoogenraad, and J. Jaworski. 2011. CLIP-170 and IQGAP1 cooperatively regulate dendrite morphology. *J. Neurosci.* 31:4555–4568. https://doi.org/10.1523/JNEUROSCI.6582-10.2011

Tirnauer, J.S., E. O'Toole, L. Berrueta, B.E. Bierer, and D. Pellman. 1999. Yeast Bim1p promotes the G1-specific dynamics of microtubules. *J. Cell Biol.* 145:993–1007. https://doi.org/10.1083/jcb.145.5.993

Umekawa, M., and D.J. Klionsky. 2012. Ksp1 kinase regulates autophagy via the target of rapamycin complex 1 (TORC1) pathway. *J. Biol. Chem.* 287:16300–16310. https://doi.org/10.1074/jbc.M112.344952

Urban, J., A. Soulard, A. Huber, S. Lippman, D. Mukhopadhyay, O. Deloche, V. Wanke, D. Anrather, G. Ammerer, H. Riezman, et al. 2007. Sch9 is a major target of TORC1 in Saccharomyces cerevisiae. *Mol. Cell.* 26:663–674. https://doi.org/10.1016/j.molcel.2007.04.020

van Breugel, M., D. Drechsel, and A. Hyman. 2003. Stu2p, the budding yeast member of the conserved Dis1/XMAP215 family of microtubule-associated proteins is a plus end-binding microtubule destabilizer. *J. Cell Biol.* 161:359–369. https://doi.org/10.1083/jcb.200211097

van der Vaart, B., C. Manatschal, I. Grigoriev, V. Olieric, S.M. Gouveia, S. Bjelic, J. Demmers, I. Vorobjev, C.C. Hoogenraad, M.O. Steinmetz, and A. Akhmanova. 2011. SLAIN2 links microtubule plus end-tracking proteins and controls microtubule growth in interphase. *J. Cell Biol.* 193:1083–1099. https://doi.org/10.1083/jcb.201012179

Van Dyke, N., J. Baby, and M.W. Van Dyke. 2006. Stm1p, a ribosome-associated protein, is important for protein synthesis in Saccharomyces cerevisiae under nutritional stress conditions. *J. Mol. Biol.* 358:1023–1031. https://doi.org/10.1016/j.jmb.2006.03.018

Weisbrich, A., S. Honnappa, R. Jaussi, O. Okhrimenko, D. Frey, I. Jelesarov, A. Akhmanova, and M.O. Steinmetz. 2007. Structure-function relationship of CAP-Gly domains. *Nat. Struct. Mol. Biol.* 14:959–967. https://doi.org/10.1038/nsmb1291

Weissmann, F., G. Petzold, R. VanderLinden, P.J. Huis In 't Veld, N.G. Brown, F. Lampert, S. Westermann, H. Stark, B.A. Schulman, and J.M. Peters. 2016. biGBac enables rapid gene assembly for the expression of large multisubunit protein complexes. *Proc. Natl. Acad. Sci. USA.* 113:E2564–E25649. https://doi.org/10.1073/pnas.1604935113

Wen, W., J.L. Meinkoth, R.Y. Tsien, and S.S. Taylor. 1995. Identification of a signal for rapid export of proteins from the nucleus. *Cell.* 82:463–473.

Wolyniak, M.J., K. Blake-Hodek, K. Kosco, E. Hwang, L. You, and T.C. Huffaker. 2006. The regulation of microtubule dynamics in Saccharomyces cerevisiae by three interacting plus-end tracking proteins. *Mol. Biol. Cell.* 17:2789–2798. https://doi.org/10.1091/mbc.E05-09-0892

Zanic, M., P.O. Widlund, A.A. Hyman, and J. Howard. 2013. Synergy between XMAP215 and EB1 increases microtubule growth rates to physiological levels. *Nat. Cell Biol.* 15:688–693. https://doi.org/10.1038/ncb2744

Zimniak, T., K. Stengl, K. Mechtler, and S. Westermann. 2009. Phosphoregulation of the budding yeast EB1 homologue Bim1p by Aurora/Ipl1p. *J. Cell Biol.* 186:379–391.